Functional Connectivity Shapes Spine Stability in the Hippocampus

Cynthia Rais[1] and J. Simon Wiegert[1,2,*]

[1] Research Group Synaptic Wiring and Information Processing, Center for Molecular Neurobiology Hamburg, University Medical Center Hamburg-Eppendorf, Hamburg, Germany

[2] Department of Neurophysiology, Medical Faculty Mannheim, MCTN, Heidelberg University, Ludolf-Krehl-Str. 13-17, Mannheim, Germany

* Correspondence to: simon.wiegert@medma.uni-heidelberg.de

ABSTRACT

Synaptic connections between neurons determine the flow of information in the brain. Changes in synaptic weight, along with synapse formation and pruning, reshape the functional connectivity of neural circuits—key mechanisms underlying learning and memory. However, the relationship between functional strength and the structural dynamics of individual glutamatergic synapses in the living mammalian brain remains poorly understood. Specifically, how spine morphology and stability relate to functional adaptations is unclear. Here, we repeatedly recorded excitatory postsynaptic calcium transients in single postsynaptic spines of CA1 neurons in response to optogenetic stimulation of presynaptic CA3 cells in awake, head-fixed mice for over 2 weeks. We found that functional connectivity predicted both the structural stability and spatial proximity of synaptic inputs. Spines with large responses exhibited larger volume and higher stability compared to non-responding spines. Over time, responses were highly variable at individual synapses, but stable at the dendritic level, suggesting that dendritic branches receive stable input despite large fluctuations at individual synapses.

INTRODUCTION

During learning, experience-dependent activity induces synaptic plasticity, modifying synaptic strength[1–3]. Most excitatory inputs in the brain form synapses on dendritic spines[4], where changes in synaptic strength are often accompanied by structural modifications[5–8]. This has led to the hypothesis that memory traces are stored at synapses[9,10] and, by extension, in dendritic spines. Among these, the Schaffer collateral/commissural synapses connecting the CA3 and CA1 regions of the hippocampus are considered as prototypical small glutamatergic synapses in the central nervous system. These synapses are crucial for long-term synaptic plasticity, which underlies the formation and consolidation of hippocampus-dependent declarative and episodic-like memories. The dynamic nature of memory formation and updating, particularly in response to a constantly changing environment[11] necessitates continual restructuring of neural networks[6,12]. This need for plasticity contrasts with the need for memory stability, raising a fundamental question: how does the brain maintain stable memory storage despite the inherent instability of synaptic connections? Several candidate mechanisms have been proposed[13], but the factors determining the longevity of dendritic spines remain only partially understood.

In the hippocampus, particularly in area CA1, the lifetime of dendritic spines has been tracked over the course of several days in order to assess the stability of synapses and their role in storing memory traces. However, findings remain inconsistent [14–17] with reported spine survival rates ranging from high stability to nearly complete turnover within a few weeks [17]. Many of these studies relied on repeated anesthesia, which is known to affect spine stability [15].

A further limitation of previous studies is that they focused on spine morphology without directly linking structural changes to synaptic function in vivo. Anatomical studies alone cannot reveal presynaptic input properties or distinguish between synaptic strength and morphological features. As a result, the relationship between connectivity strength and spine turnover in the hippocampus remains largely unexplored.

In this study, we used chronic two-photon calcium imaging of dendritic spines in the ipsilateral CA1 (ilCA1) region of awake mice while repeatedly stimulating presynaptic contralateral CA3 (clCA3) pyramidal neurons with optogenetics. This approach enabled us to monitor localized, synaptically evoked calcium responses at individual spines and evaluate their functional and morphological stability for over two weeks.

Our findings revealed that functionally active spines, which showed synaptically evoked calcium transients tended to form stronger and more stable connections compared to spines that did not show any synaptically evoked calcium transients. These results suggest that robust synaptic connectivity is associated with enhanced spine persistence. Overall, our results indicate that spine lifetime in the hippocampus is closely linked to synaptic strength, which may be critical for maintaining long-term synaptic connectivity.

RESULTS

Identification of post-synaptic CA1 neurons by optogenetic stimulation of pre-synaptic CA3 neurons.

To identify ilCA1 spines connected to clCA3 neurons, we sparsely labelled ilCA1 pyramidal neurons in adult mice with a Cre-dependent calcium sensor, jGCaMP7b, and implanted a chronic hippocampal window. To elicit pre-synaptic action potentials, we densely expressed the red light-activated optogenetic actuator ChrimsonR in clCA3 pyramidal neurons followed by the implantation of an optic fiber (Figure 1a, S1a). We estimated the light distribution in area CA3 using a Monte Carlo simulation [18] considering light scattering and absorption at 633 nm and the optical properties of the light fiber (200 um, 0.22 NA). Given the modeled distribution of light intensities and the spike thresholds for ChrimsonR [19], we assume that we reliably stimulated the entire clCA3, including distal and medial regions (Figure S1b-d). Most of the distal and medial CA3 cells project to the stratum oriens [20]. Therefore, we expect a large portion of their axons to terminate in the stratum oriens of CA1 – also on the ipsilateral side, where imaging occurred. In fact, Schaffer commissural axons from the contralateral CA3 region comprise approximately 50% of the synaptic input, preferentially terminating in the stratum oriens of the ipsilateral CA1 region [21]. Therefore, by imaging spines in the stratum oriens of the ipsilateral CA1, we expect to reliably detect postsynaptic responses to optogenetic stimulation of the contralateral CA3 (Figure S1e-f).

During two-photon spine imaging, we recorded the motion of head-fixed mice using a passive treadmill, enabling closed-loop optogenetic stimulation selectively during periods of immobility, when motion artefacts were largely absent (Figure 1b). Accurate, continuous monitoring of locomotion via the treadmill was essential to prevent brain-motion artefacts that can lead to out-of-focus signals (Figure S1g-h). This closed-loop approach allowed us to exclude motion-affected frames while maximizing the number of trials without motion artefacts.

Before starting the chronic spine imaging, we first identified ilCA1 neurons receiving reliable synaptic input from clCA3 neurons (Figure 1c). Given that only a fraction of presynaptic CA3 was stimulated with our approach (i.e., contralateral CA3 neurons) this ensured that we focus on those CA1 neurons that display a high fraction of functionally stimulated synapses, facilitating the detection of responding spines. Upon strong optogenetic stimulation in clCA3, a subset of ilCA1 neurons showed large, invariant calcium transients, while the remaining ilCA1 did not show detectable suprathreshold calcium events (Figure 1d-e). The robust and reproducible responses in individual ilCA1 cells indicate that synaptic input from optogenetically activated clCA3 neurons was reliable, without leading to unspecific, global activation of the entire CA1 region. By injecting five adult mice with ChrimsonR in clCA3 and non-conditional jGCaMP8m in ilCA1 for dense labelling, we further confirmed that optogenetically evoked synaptic input to ilCA1 was maintained constant across imaging sessions (Figure S2). In this way, we could detect the population response in ilCA1 without being biased towards a small number of sparsely labeled neurons. We stimulated clCA3 neurons using the same protocol and imaging timeline (Figure 1c) and chronically recorded synaptically evoked calcium responses from the same population of ilCA1 neurons. We did not find any systematic changes in the mean amplitude over time, suggesting that overall optogenetically evoked synaptic transmission remained stable (Figure S2c-d). Thus, our experimental protocol enabled us to optogenetically evoke stable synaptic transmission at Schaffer commissural synapses in awake mice during a time period of more than two weeks.

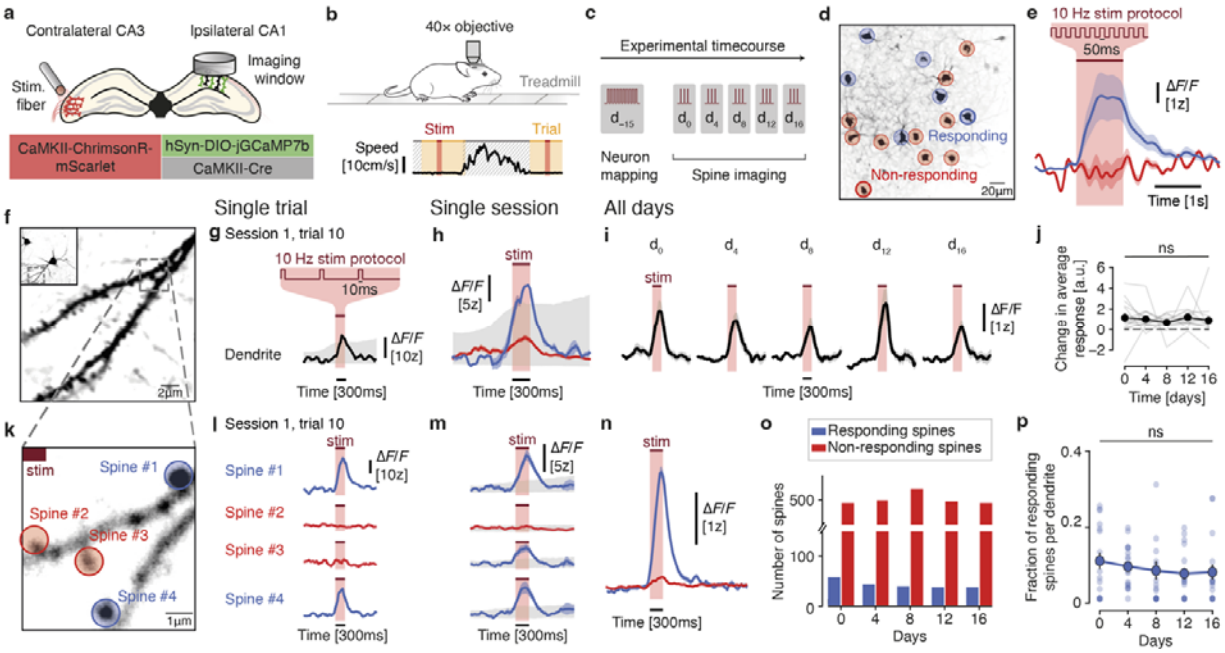

Figure 1 Identification of synaptically connected CA1 neurons by optogenetic stimulation of pre-synaptic CA3 neurons. A) Schematic illustration depicting injections in cICA3 and iICA1 for sparse labelling and chronic implants for stimulation and imaging. **B)** Schematic illustration of closed-loop, two-photon recording configuration of a mouse on a treadmill with automated motion detection. **C)** Time-course of the experiment. **D)** Example field of view with neurons responding (blue) or not responding (red) to optogenetic stimulation. **E)** Mean EPSCaTs from responding (blue) and non-responding (red) neurons in (d). Mean ± s.e.m. N=6 responding neurons and 10 non-responding neurons. **F)** Example field view showing a dendrite from the neuron in the inset. **G)** Example EPSCaT in the dendrite in a single optogenetic stimulation trial. Shaded grey indicates the result from the permutation test. **h)** Average responses from successfully (blue) and non-successfully (red) evoked EPSCaTs in the dendrite in (f). Mean ± s.e.m. Shaded grey indicates the result from the permutation test. **i)** Average EPSCaTs measured at the same dendrite every four days. Mean ± s.e.m. **j)** Changes in the average amplitudes of EPSCaTs in all dendrites (gray lines). Linear Mixed Model with dendrites as random effect. Mean ± s.e.m. N=17 dendrites, 5 mice. **k)** Zoomed-in view of dendritic segment shown in (f) during the optogenetic stimulation trial in (g). **l)** Calcium recordings of four spines labeled in (k) during a single trial as in (g). Only spines #1 and #4 showed EPSCaTs. **m)** Average EPSCaTs from the four spines in (f) and (g). Three spines were classified as responding (blue) and one as non-responding (red) during this session. Mean ± s.e.m. Shaded grey indicates the result from the permutation test. **n)** Average EPSCaTs of all responding (blue) and non-responding spines (red) in one session. **o)** Number of all responding (blue) and non-responding (red) spines over time. **p)** Fraction of responding spines per dendrite over time. Linear Mixed Model with dendrites as random effect. N=17 dendrites, 5 mice.

Local spine calcium responses are evoked by subthreshold optogenetic stimulation of pre-synaptic neurons.

Since we aimed to investigate structural plasticity in functionally connected spines, we optogenetically stimulated CA3 neurons to evoke excitatory postsynaptic calcium transients (EPSCaTs) in postsynaptic CA1 spines. EPSCaTs depend on depolarization by AMPA receptors[22] and they are largely mediated by NMDA receptors[23] with contributions from voltage-gated calcium channels[24] and intracellular stores in some cases[25]. EPSCaTs are indicative of synaptic strength[26,27] and they were recently shown to reliably report glutamatergic synaptic transmission at CA1 pyramidal neurons in vivo[28]. Thus, EPSCaTs serve as a good proxy for postsynaptic responses at spines of CA1 pyramidal neurons.

To ensure that we can detect EPSCaTs reliably, we aimed to avoid triggering strong global calcium transients in the entire ilCA1 neuron, which could arise from suprathreshold depolarization and action potential back propagation. The protocol was set to an intensity, such that most trials remained sub-threshold, triggering dendritic events only in a small number of trials (5.90 ± 0.90 %) (Figure 1f-h). Keeping the stimulation protocol constant, we then chronically recorded EPSCaTs in the same spines every four days over the course of 16 days (see timeline in Figure 1c). To verify the reliability of our adjusted optogenetic stimulation paradigm, we first measured the average calcium transients over all trials across the entire dendrite, including suprathreshold events and all responding spines. Average calcium transients were similar across days (Figure 1i-j), validating the stability and consistency of optogenetically evoked synaptic transmission in ilCA1.

To evaluate the individual synaptically evoked calcium events for a given spine, the contribution of dendritic events was subtracted[29,30]. This method was effective in eliminating occasional weak dendritic calcium events that would lead to false-positive EPSCaTs in spines that did not receive synaptic input. We thus could identify ilCA1 spines that received inputs from optogenetically stimulated clCA3 neurons (Figure 1k, l, S1f). As expected from the low release probability of Schaffer commissural synapses, spines were not showing EPSCaTs at every trial. By averaging all trials of the entire session, we could identify ilCA1 spines receiving functional input from optogenetically stimulated clCA3 cells and discriminate them from spines not responding in that session (Figure 1m, n).

When systematically following the same spines over time (every four days), we observed that most spines responded only in one session and remained silent in preceding or following sessions. (Figure S3a, b). A small fraction of spines showed responses in two (12.0%), three (4.6%) or four (1.1%) sessions (Figure S3b). A majority of spines showed a first response in the first imaging session (approx. 1/3 of all spines ever showing a response). Accordingly, spines showing EPSCaTs for the first time were also found in later sessions, with an equal distribution across those sessions (Figure S3c). The bias towards the first session is inherent to the experimental approach: by default, any responding spine in this session is classified as responding for the first time, since no preceding sessions exist. In addition, since we screened for dendrites with active spines in the first session, this may also have contributed to a higher fraction. In the following sessions, the same dendrites were revisited irrespective of spine responses. Nevertheless, the variability in responses (i.e., spines not responding in all sessions or even functionally emerging in later session) suggests that functional connectivity gets reconfigured between sessions and therefore, individual synaptic inputs drift over time.

Given the observed drift at the single-synapse level, we investigated whether the total fraction of responding spines per session remained stable across days, which would ensure the preservation of average synaptic input, as suggested by the overall stability of dendritic responses (Figure 1j). Indeed, both the total number (Figure 1o) and relative dendritic fraction (Figure 1p) of responding spines remained consistent across sessions, indicating stable dendritic input. This finding is further supported by the invariant spine density across all sessions (Figure S3d).

Together, these results demonstrate that, while individual synaptic inputs from clCA3 neurons exhibited high temporal variability, the overall dendritic input remained stable throughout the experiment.

Responsive spines are strongly connected to pre-synaptic partners.

Next, we grouped all spines into two categories: spines that exhibited optogenetically evoked post-synaptic calcium responses at least in one session ("responsive spines") and spines that were classified as non-responding across all sessions ("unresponsive spines", Figure 2a, see Methods for details).

We then asked whether responsive spines constituted stronger synapses than unresponsive spines. The latter group may include either weakly connected synapses of optogenetically stimulated CA3 neurons or synapses of CA3 neurons that were not stimulated (e.g., ipsilateral CA3 neurons). Because spine volume is widely considered a proxy for synaptic strength[7,31,32], we estimated the head volumes of both responsive and unresponsive spines (Figure 2b). Responsive spines were significantly larger than unresponsive spines (Figure 2c, Figure S4), suggesting that, on average, they were more strongly connected to their presynaptic partners.

However, because unresponsive spines may also include strong synapses that were not activated, we next restricted our analysis to responsive spines to avoid confounds associated with synapses of unknown activation status. We tested whether spine volume correlated with the amplitude of excitatory postsynaptic calcium transients (EPSCaTs). Indeed, we observed a positive correlation between spine volume and EPSCaT amplitude (Figure 2d), consistent with previous findings that larger spines correspond to stronger synapses[33]. Thus, although unresponsive spines likely represent a heterogeneous population with a broad distribution of synaptic strengths, our results indicate that responsive spines preferentially correspond to strong synapses.

To ensure that our spine volume estimates were not influenced by intracellular calcium levels, we acquired volumetric stacks at an isosbestic (calcium independent) excitation wavelength (Figure S5a). We observed a strong correlation between the two measures (Figure S5b), indicating that both strategies yielded comparable volume estimates. In addition, we also controlled for the relationship between the volume obtained from the time-series for all spines and calcium fluctuations (Figure S5c). We did not find a significant correlation, suggesting that volume measurements were not confounded by dynamic brightness changes arising from intracellular calcium dynamics. Finally, we asked whether spine volume was directly related to the presence of calcium responses within individual imaging sessions. To address this, we subdivided all responsive spines into sessions in which a calcium response was detected and sessions in which no response was observed, and compared the corresponding spine volumes. We found no significant effect of response presence on measured spine volume, although we observed a weak trend toward slightly larger volumes during responding sessions (Figure S5d). Thus, while spine volume correlated with EPSCaT amplitude across spines, this relationship was only weakly expressed within individual spines across sessions, likely reflecting a non-linear relationship between calcium transients, synaptic strength, and spine morphology.

Next, we investigated the dendritic distribution of responsive spines. Previous studies suggest that synaptic clustering can enhance local dendritic integration, potentially leading to cooperative synaptic potentiation[20,22,23]. Moreover, due to their highly divergent connectivity, CA3 neurons form only a small number of synapses with a given CA1 neuron. These synapses are often found in close proximity to each other, given that they arise from the same presynaptic axon branch[35]. To assess whether responsive spines were in closer proximity to each other compared to all other spines, we measured all-to-all dendritic distance between the spines in the field of view (Figure 2e). Our comparison of the spatial distribution of responsive and all other spines revealed a closer spatial proximity (shorter dendritic length) between responsive spines versus unresponsive spines (Figure 2f). This suggests – as expected from CA3-CA1 connectivity – that functional inputs from a defined population of pre-synaptic neurons are more likely to be in spatially closer proximity rather than randomly distributed[36].

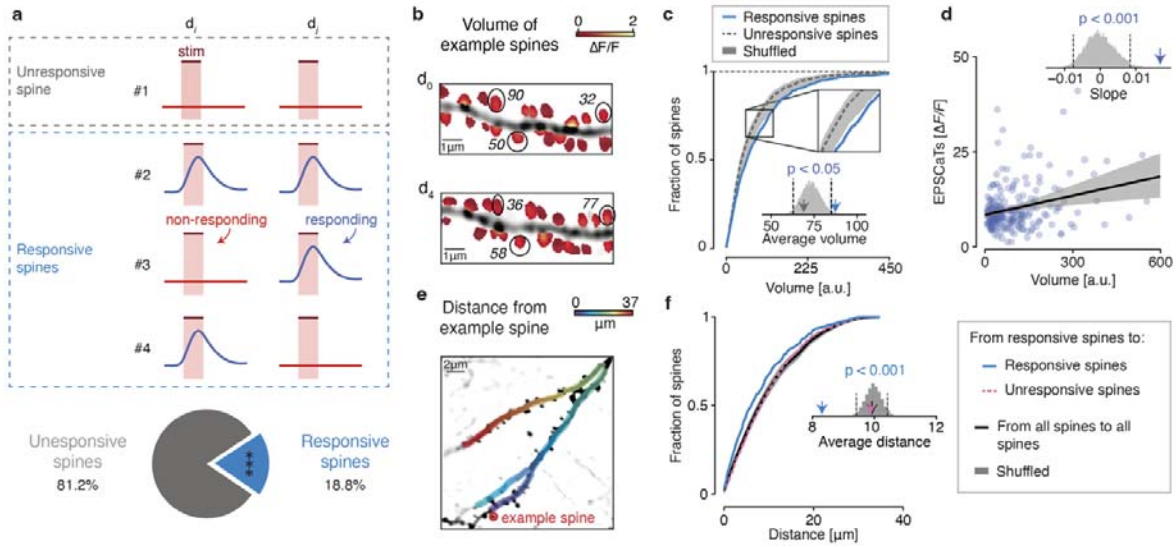

Figure 2 Responsive spines display strong synaptic connections. a) Definition of responsive and unresponsive spines and their fractions in the total pool of analyzed spines. Top: an unresponsive spine was classified as non-responding in all sessions (#1), while responsive showed EPSCaTs in at least one imaging session (#2-4). Bottom: total fraction of responsive spines. N=175 responsive spines and 754 unresponsive spines, 17 dendrites, 5 mice. Binomial test. ***: $p < 0.001$. **b)** Example of relative spine volumes on a dendrite at two different timepoints. The relative volume was derived by normalizing total spine fluorescence to dendrite fluorescence (see Methods). **c)** Cumulative distributions of spine head volumes of responsive (blue) and unresponsive (dark grey) spines. Inset: Shuffled volumes indicated by grey histogram. Arrows indicate average spine volumes. Permutation tests. N=175 responsive spines and 754 unresponsive spines, 17 dendrites, 5 mice. **d)** EPSCaTs amplitude as a function of the volume of responsive spines. Top: arrow indicates slope and grey histogram shows shuffled relationship between EPSCaTs and volume. Pearson correlation: 0.27. Permutation tests. N=175 responsive spines, 17 dendrites, 5 mice. **e)** Dendritic path length (distance) between a given spine (example spine) and all other spines. The color code indicates the distance between the example spine and all other spines present along the dendritic segment. **f)** Cumulative distributions of distances between spines. Inset: Shuffled distances indicated by grey histogram. Arrows indicate average differences between spine categories. Permutation tests. N=175 responsive spines and 754 unresponsive spines, 17 dendrites, 5 mice.

Responsive spines display increased stability

Since responsive spines were on average larger than randomly selected unresponsive spines, and given the positive correlation between spine volume and postsynaptic responses, we asked whether they also exhibited greater stability over time. Spines were categorized into four dynamic categories: (1) **persistent** spines, present throughout the entire time series; (2) **transient** spines, which appeared temporarily and then disappeared again; (3) **formed** spines, which emerged during the time series and remained until the end; and (4) **eliminated** spines, present at the beginning but disappearing before the end of the time series (Figure 3a).

Independently, we categorized spines as either responsive or unresponsive and analyzed their distribution across the four groups. We found that responsive spines exhibited a higher proportion of persistent spines and a lower proportion of transient spines compared to unresponsive spines (Figure 3b). - Transient spines in the responsive group were more likely to reappear at the same dendritic location on different days (i.e., they were recurrent) compared to transient unresponsive spines (Figure 3c). Recurrence was lower in the population of transient, unresponsive spines. Despite this, the frequency of flips (disappearance and reappearance) was similar between transient responsive and unresponsive spines. This recurrence in responsive spines may be

explained by repeated stimulation, which could act as a stabilizing signal for the synapse[37,38], promoting the regrowth of otherwise retracting spines.

To further characterize the dynamics of responsive and unresponsive spines, we analyzed different properties related to their life expectancy in more detail. First, we separately assessed the turnover ratio for responsive and unresponsive spines in each imaged dendritic segment. For both groups (responsive or unresponsive spines), the turnover ratio is defined as the sum of spine formation and spine elimination rates between consecutive imaging sessions. Consistent with the higher fraction of persistent spines in the responsive population, the turnover ratio was lower for responsive spines at each imaging interval (Figure 3d). Since the turnover ratio depends on both formation and elimination rates, we analyzed both parameters separately (Figure S6). We found that both the formation and elimination rates of responsive spines were lower compared to unresponsive spines (Figure S6a), as expected, given the larger population of stable responsive spines.

The turnover ratio, including formation and elimination rates when analyzed individually, remained invariant within both populations (i.e., responsive and unresponsive spines), indicating that optogenetic stimulation did not directly influence spine stability. This conclusion was further supported by comparing the stability of all spines in the group of optogenetically stimulated animals to spines on dendrites from control animals not undergoing optogenetic stimulation (Figure S7). We did not observe any differences in the distribution of the dynamic categories, persistent, transient, formed, eliminated nor in the turnover ratio, or survival fraction between the two treatment conditions (Figure S7 a-c). Thus, similar to optogenetically stimulated dendrites (Figure S3d), the spine density on control dendrites remained stable over days (Figure S7d). Finally, the volume of non-stimulated control spines was not significantly different from responsive and unresponsive spines in optogenetically stimulated mice (Figure S7e). Together with the stable amplitude of EPSCaTs in dendrites (Figure 1i), these results confirm that the optogenetic stimulation used to identify synaptic connections did not induce significant changes in spine stability or structure over time.

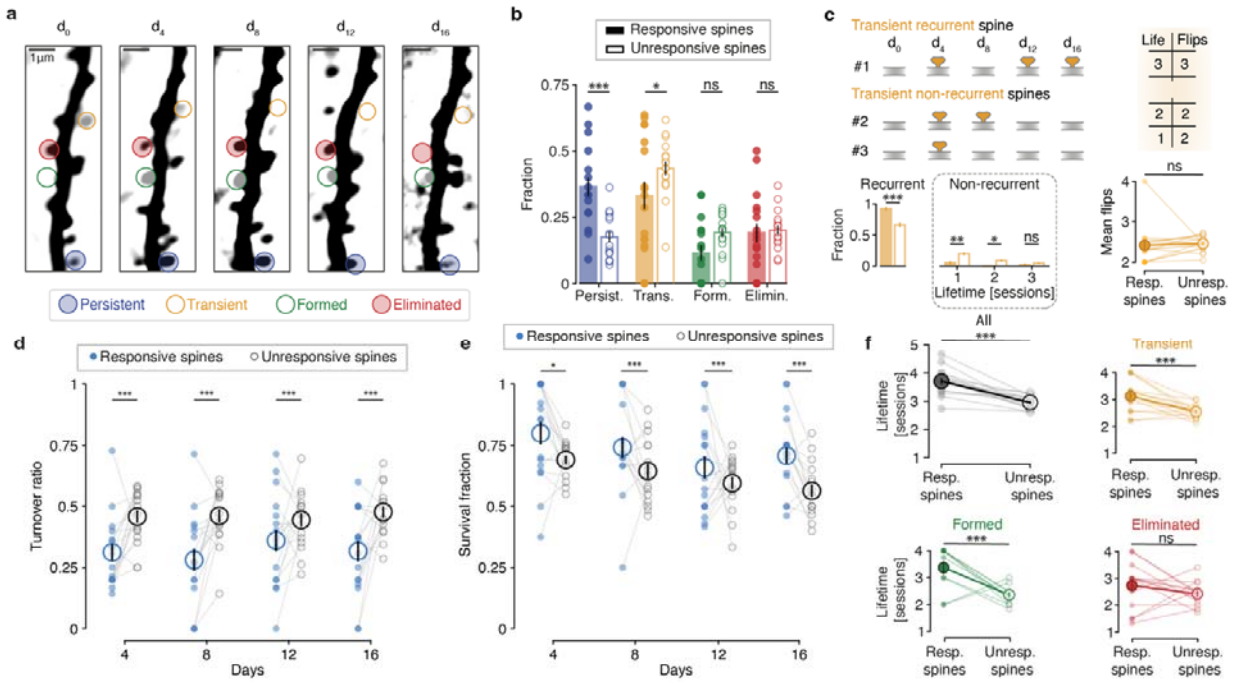

Figure 3 Enhanced stability of responsive spines. a) Example dendrite imaged every four days. Examples of persistent (blue), transient (yellow), formed (green), and eliminated (red), spines are indicated by colored circles. **b)** Fractions of the different categories for responsive (filled circles) and unresponsive spines (empty circles). Linear Mixed Model with dendrites as random effect and pairwise comparisons with Bonferroni correction. Each circle represents a dendrite. **c)** Characteristics of transient spines. "Life": Cumulative lifetime in days. "Flips": Number of appearance and disappearance events. Linear Mixed Model with dendrites as random effect and pairwise comparisons with Bonferroni correction. Mean ± s.e.m. **d)** Turnover ratio of responsive spines versus unresponsive spines in a dendritic segment between two sessions. Pairs of filled and open circles connected by a line represent responsive and unresponsive spines on a given dendrite. Linear Mixed Model with dendrites as random effect and pairwise comparisons with Bonferroni correction. Mean ± s.e.m. **e)** Survival fraction of responsive spines versus unresponsive spines at each session. Pairs of filled and open circles connected by a line represent response and unresponsive spines on a given dendrite. Linear Mixed Model with dendrites as random effect and pairwise comparisons with Bonferroni correction. Large circles: mean ± s.e.m. **f)** Lifetime of responsive (filled circles) and unresponsive spines (empty circles) sorted by category. Categories colored as in (b). Linear Mixed Model with dendrites as random effect. ns: non-significant, * : $p < 0.05$, ** : $p < 0.01$, *** : $p < 0.001$.

A high turnover ratio could potentially result from a high formation rate of new spines without affecting the stability of existing spines. To explore this in more detail, we assessed the survival fraction defined as those spines detected in a given imaging session that were present in all preceding imaging sessions from the beginning. The survival fraction of responsive spines was consistently higher than that of unresponsive spines, further highlighting their greater stability (Figure 3e). The increased stability and extended lifetime of responsive spines (Figure 3f) may largely be attributed to the higher proportion of persistent spines in this population. To investigate whether spine lifetime is generally higher when spines are responsive, we specifically measured the lifetimes of all non-persistent spines (i.e., transient, formed, and eliminated spines). Remarkably, spines that formed during the experiment (transient and formed spines) exhibited longer average lifetimes when they were responsive to presynaptic optogenetic stimulation (Figure 3f). These findings suggest that responsive spines, which tended to be stronger than unresponsive spines, also exhibited a longer overall lifetime.

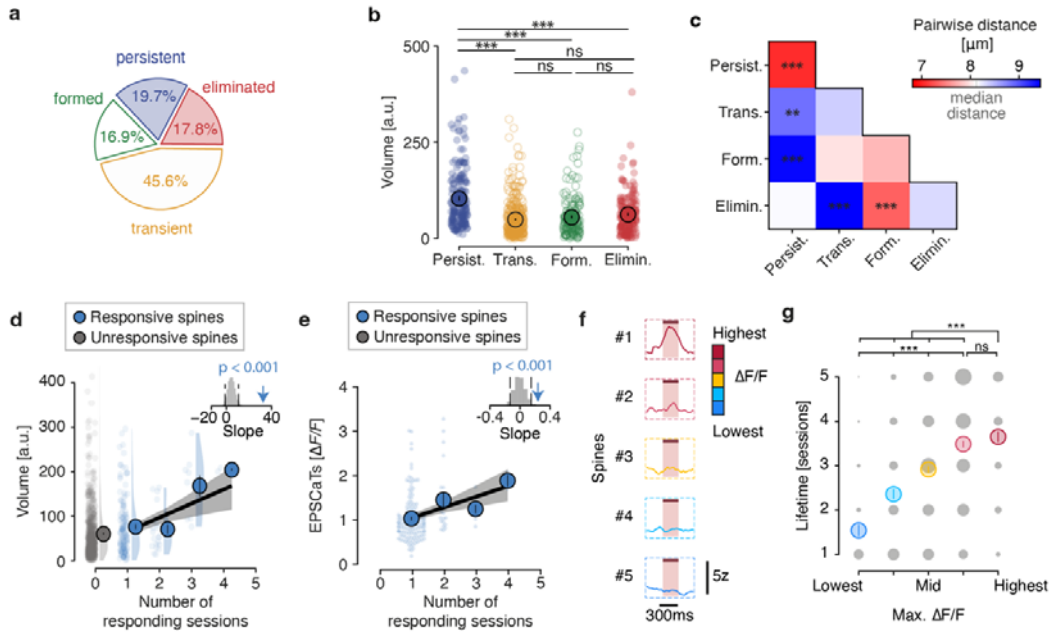

Fig 4. Persistent spines are larger, more proximal to each other, and show larger EPSCaTs compared to non-persistent spines. a) Percentages of the different dynamic categories of all imaged spines. N=929 spines, 17 dendrites, 5 mice. **b)** Head volumes of the different dynamic spine categories. N=929 spines, 17 dendrites, 5 mice. Permutation tests. **c)** Pairwise distances between spines of the different dynamic spine categories. N=929 spines, 17 dendrites, 5 mice. Permutation tests. **d)** and e) Spine head volume (d) or EPSCaT amplitude (e) as a function of the number of sessions in which the spine responded. Shuffled data indicated in shaded grey. Top right: arrow indicates slope and grey histogram shows shuffled relationship between volume (d) or EPSCaT amplitude (e) and the number of responding sessions. Permutation tests. N = 175 responsive spines, 17 dendrites, 5 mice. **f)** Example traces of the spines sorted according to their maximal ΔF/F irrespective of their categorization as responsive or unresponsive. **g)** Lifetime of the spines depending on the categories of maximal ΔF/F. N=929 spines, 17 dendrites, 5 mice. Permutation tests. ***: $p < 0.001$, **: $p < 0.01$, ns: non-significant.

To validate this relationship independently of optogenetically identified spines, we categorized all spines—regardless of their activity—again into the four dynamics categories persistent, transient, formed, and eliminated, hypothesizing that persistent spines would exhibit larger volumes, indirectly suggesting that they are stronger than non-persistent ones. 19.7% of all spines were classified as persistent, while nearly half were transient (45.6%). The remaining spines were divided almost equally between formed (16.9%) and eliminated (17.8%) categories (Figure 4a). As expected from the responding spine population and in agreement with previous work[32], persistent spines were significantly larger than spines in all other non-persistent categories (Figure 4b, Figure S8).

We also analyzed the spatial distribution of the four spine categories and found a shorter distance between persistent spines compared to their distance to other spines (Figure 4c, Figure S9a), suggesting that persistent spines tended to be closer together. In comparison, no difference to the overall median pairwise distance was found in the distance between transient, eliminated or formed spines. Notably, newly formed and transient spines were more distal to persistent spines. Instead, newly formed spines appeared closer to the location of eliminated spines, suggesting that they appeared in places where preexisting spines were lost. Conversely, transient spines were distant to eliminated spines.

In conclusion, persistent spines showed higher proximity to each other and were generally larger than non-persistent spines of all categories – suggesting a stronger connection to their pre-synaptic partners, while non-persistent spines were likely less strongly connected and more randomly

distributed. This analysis further corroborates the positive relationship between synaptic strength, size, and stability.

We have established a relationship between synaptic strength (EPSCaT amplitude) and spine volume in vivo (Figure 2e). Moreover, we showed that spines displaying a postsynaptic response to presynaptic optogenetic stimulation are more persistent than unresponsive spines (Figure 3) and that stable spines display a larger head volume (Figure 4), indirectly suggesting that larger spines belong to stronger synapses, which, in turn, display higher stability. To establish this relationship between synaptic strength, spine volume and spine stability more firmly, we asked if the frequency of synaptic responses (i.e. the number of imaging sessions in which spines showed EPSCaTs) is related to EPSCaT amplitude and spine head size. We found a significant positive correlation between the frequency of responses and the average volume of responding spines as well as EPSCaT amplitude (Figure 4d, e).

Because our categorization into responsive and unresponsive spines could have led to the exclusion of weakly responsive spines, we considered again all imaged spines and split them into five categories according to their highest maximum fluorescent transients across all sessions, including all spines that were previously categorized as unresponsive (Figure 4f). This alternative analysis confirmed the relationship between the maximal calcium response and the spine lifetime (Figure 4g). Thus, our data demonstrate a close relationship between spine size, functional connectivity and spine stability at hippocampal CA3-CA1 synapses *in vivo*.

DISCUSSION

In this study, we demonstrated that the stability of glutamatergic spines at CA3-CA1 synapses in the hippocampus is regulated by connectivity strength. Using chronic two-photon imaging of spines in ilCA1, combined with optogenetic stimulation of presynaptic clCA3 neurons, we discovered that spines that exhibited robust postsynaptic calcium responses displayed increased size, a longer lifetime, and a closer spatial proximity to each other compared to neighboring spines that did not exhibit detectable postsynaptic calcium responses.

Previous studies in anesthetized mice have reported a wide range of spine dynamics at CA1 basal dendrites in vivo[14–16]. However, these studies have only assessed anatomical features without linking spine turnover with their functional properties. Therefore, it remained unclear to what extent functional and morphological properties, such as synaptic weight or spine volume, would predict spine stability at hippocampal synapses in vivo. By tracking functionally identified spines over more than two weeks in awake mice, we established a link between spine lifetime and connectivity strength, while avoiding the confounding effects of repeated anesthesia[15]. Spines with a strong functional connection (i.e. responsive spines) not only exhibited a larger head volume but also showed a lower turnover ratio, which was due to an increased survival rate and thus, an enhanced lifetime compared to their non-responsive neighbors. This work is in line with a previous study, showing a correlation between spine lifetime and spine size[16]. In addition to the increased stability of responsive spines we also found a correlation between the propensity of responses and spine volume, indicating that the stability of functional connectivity directly influences the weight and thereby, the persistence of a synapse, as previously suggested by anatomical studies[13,39,40].

The larger head volume of responsive spines compared to unresponsive neighboring spines indicates a stronger synaptic connection[7,31,32] with pre-synaptic clCA3 neurons. Those spines could belong to functional ensembles, which previously underwent LTP[41,42] as suggested by a previous report[36]. We observed a slightly higher spatial proximity between strong, responsive synapses, which may indicate that small groups of spines receive input from the same presynaptic CA3 cells or from CA3 cells with similar functional tuning. These strong inputs may have contributed to postsynaptic calcium responses in CA1 neurons during our initial screening (Figure 1c-e) by contributing sufficient depolarization to reach cellular spike threshold[42]. Notably, the proximity of responsive spines in our study does not represent anatomical clusters. This is likely due to the fact that we stimulated only a subset of all CA3 cells providing direct synaptic input to the postsynaptic CA1 cell. Thus, only a fraction of all spines on a given dendritic segment receives direct, optogenetically evoked input, while other synapses on the same dendrite may originate from non-stimulated CA3 cells, which remain elusive during postsynaptic calcium imaging. Functional clusters might only be revealed by activity of all presynaptic neurons that share functional properties, as is the case during spatial navigation where spatially tuned CA3 cells are co-active in a given dendritic location[43,44]. Nonetheless, the closer spatial proximity of responsive spines aligns with findings from those recent studies demonstrating that spine clusters on place cells were correlated with the spatial tuning of these neurons during a spatial navigation task[45]. As a consequence, such clustering of functionally related spines likely contributes to neuronal firing within specific place fields, consistent with prior studies that have linked functional spine clustering to learning[31,34,43,44]. Due to their increased stability, such synaptic populations can form long-lasting ensembles with a feature-specific presynaptic population of CA3 cells. This helps to stabilize specific synaptic input to a feature-selective CA1 cell (e.g., place cell firing) over time despite fluctuations at individual synapses.

Our stimulation paradigm induced local synaptic EPSCaTs in postsynaptic spines of CA1 neurons. A potential limitation of this method is its reliance on voltage-gated calcium entry[23–25,27,46] which only indirectly reports glutamatergic synaptic transmission. Thus, weak synapses or spines

with low AMPA receptor density may not reach sufficient depolarization to unblock NMDA receptors or open voltage-gated calcium channels. Therefore, weakly connected synapses might have fallen under the detection threshold and therefore gotten classified as unresponsive spines. Consequently, the absence of spine calcium responses can have two reasons. Either the spine belonged to a weak, stimulated synapse, which did not elicit suprathreshold postsynaptic calcium transients due to insufficient depolarization, or the spine received input from a non-stimulated CA3 cell. Thus, unresponsive spines likely represent a mixed population of synapses of various strengths. Importantly, a recent study in awake mice showed that EPSCaTs in CA1 spines reliably reported glutamatergic transmission, suggesting that EPSCaTs are suitable to monitor excitatory transmission at Schaffer collateral/commissural synapses. Moreover, since EPSCaTs depend on depolarization by AMPARs[22] they are indicative of synaptic strength[26] . A relationship between synaptic strength and EPSCaTs was further demonstrated in vivo via simultaneous spine voltage imaging[47]. Therefore, EPSCaTs most likely scale with synaptic weight[48,49]. This relationship is further underlined by the positive correlation between EPSCaT amplitude and spine volume observed in this study. Thus, synapses that showed robust EPSCaTs were considered strong synapses, while synapses that did not exhibit EPSCaTs were either weak or they belonged to a pool of non-stimulated synapses with undetermined strength. To avoid any potential confounds associated with the classification into responsive and unresponsive spines we sorted all synapses according to their maximal fluorescence transients and also analyzed their lifetime, which confirmed that spines with large calcium responses had a higher survival rate (Figure 4f).

Overall, 19% of all recorded spines displayed robust calcium responses. Notably, responsive spines exhibited EPSCaTs primarily in a single imaging session, suggesting dynamic functional reconfiguration of connectivity across sessions. This reconfiguration may reflect changes in synaptic connectivity strength, wherein both spontaneous fluctuations in presynaptic AP-evoked transmitter release[50] and fluctuations in postsynaptic calcium responses could contribute to the transient loss of detectable EPSCaTs at weaker synapses. Future studies aiming to directly study the influence of synaptic plasticity on synapse dynamics and spine stability in the hippocampus, similar to prior in vitro research[48,49,51] need to overcome challenges associated with classical plasticity-induction protocols[49,52] such as high-frequency or burst stimulation *in vivo*. In our hands, such protocols strongly altered network dynamics and led to perception of this overall altered network state by the animal. This made it impossible to dissociate pathway-specific plasticity from global alterations of network states. Refined and spatially restricted stimulation protocols with better temporal control, for example, via holographic 2P-stimulation may help to overcome such limitations in the future and help to better understand the influence of long-term potentiation and depression on spine stability *in vivo.* Another strategy to circumvent artefacts associated with plasticity-inducing stimulation protocols is to rely on sensory stimuli[53] or to pair naturally occurring synaptic input with postsynaptic manipulation of neuronal activity[47,54]. Recent studies have employed postsynaptic optogenetic stimulation of CA1 cells to induce behavioral time scale plasticity followed by functional measurements of naturally occurring synaptic transmission[47,55]. While these studies linked synaptic plasticity to cellular function in vivo, they did not follow the functional or structural properties of these synapses over time. Thus, future functional and structural studies of identified spines associated with a specific behavior or a cellular function over extended time periods will be important to shed light on the role of individual synapses in long-term information processing and storage in the brain. Indirect evidence suggests that spine stability is increased at CA1 neurons, which are part of an engram[56]. Directly assessing the lifetime of spines involved in the control of these neurons and concurrent animal behavior would provide critical insights into the synaptic mechanisms underpinning memory encoding and storage within the neuronal networks involved in episodic memory formation and storage[57].

METHODS

Animals. Adult (2 to 9 months of age) C57BL/6J mice of both sexes were used in this study. The mice originated from the Charles River company and were housed under pathogen-free conditions at the University Medical Center Hamburg-Eppendorf with a light/dark cycle of 12/12 hours. The humidity and temperature in the room were kept constant (40% relative humidity; 20°C). Food and water were available ad libitum. All procedures were performed in compliance with German law according and the guidelines of Directive 2010/63/EU. Protocols were approved by the Behörde für Gesundheit und Verbraucherschutz of the City of Hamburg under the license numbers 32/17 and 33/19.

Mouse surgery and virus injections. C57BL/6J wild-type mice were anesthetized with 2% isoflurane/1L of O_2. After 5 minutes, mice were transferred to the stereotaxic frame, and anesthesia was maintained with 1.5% isoflurane/1L of O_2. To evaluate the depth of anesthesia and analgesia, the paw withdrawal reflex test was performed with a toe-pinch. Upon deep anesthesia, Buprenorphine (0.1 mg/kg) and Carprofen (4 mg/kg) were injected subcutaneously. The mouse kept on a heating pad throughout surgery to maintain the body temperature and eye ointment (Vidisic, Bausch + Lomb) was used to prevent eye drying. The fur on the head was trimmed and carefully removed to avoid later contamination in the surgical field. The skin was disinfected using Betaisodona. The mouse was then fixed in the stereotaxic frame and a 3-4cm midline scalp incision was made close to the injection sites. The skin was pushed to the side and a bone scarper was used for cleaning (Fine Science Tools). Above the injection sites, two holes were made using a dental drill (Foredom). 0.3µL of AAV9-CaMKII-ChrimsonR-mScarlet-KV2.1 (1×10^{13} vg/mL, AddGene # 124651-AAV9) viral suspension was first injected in left CA3 (-2.0mm AP, -2.3mm ML, -2.5mm DV relative to Bregma) using a custom-made air-pressure driven injection system. For the spine recording experiments, 0.5µL of a 1:1 mix of AAV9-CaMKII-Cre (3×10^{9} vg/mL, gift from D. Kuhl) and AAV1-Syn-flex-jGCaMP7b-WPRE ($1{,}4\times10^{13}$ vg/mL, AddGene #104493-AAV1) or AAV9-hsyn-DIO-GCaMP7b-P2A-GSG-mRuby3 ($8{,}15\times10^{13}$ vg/mL, AddGene #130900) was injected in right CA1 (-2.0mm AP, +1.5mm ML, -1.5mm DV relative to Bregma). In experiments where dense CA1 cellular recording were done, mice were instead injected with 0.5µL of AAV9-Syn-jGCaMP8m (4×10^{12} vg/mL, AddGene #162375-AAV9) in CA1. The scalp was sutured after injections were completed. Mice were removed from anesthesia and allowed to recover in a clean cage on a heating blanket. During the following three days, mice were provided with Meloxicam mixed into soft food.

After a recovery period of at least two weeks, implantation of a hippocampal imaging window together with a contralateral light fiber took place. Mice were anesthetized as described above. After the removal of fur, the skin covering the implantation sites was removed. The skull was cleaned and roughened with a bone scraper. A first hole using the dental drill was made over the left CA3 (-2.0mm AP, -3.5mm ML, titled 35° towards the left) and an optic fiber (200µm, NA 0.22, 1.25mm ferrule diameter, 1.3 ± 0.1mm length, Doric Lenses) was inserted and glued to the skull. Once the glue had dried, a circular 3mm bone piece, centered on the CA1 injection site, was carefully removed using a trephine (MW Dental, ISO 020). The dura and somatosensory cortex above the hippocampus were carefully aspirated until the fiber tracts of the corpus callosum became visible. Sterile PBS was used to wash the craniotomy all along, and a custom-made hippocampal imaging window was inserted. To build the window, a hollow glass cylinder was glued to a No. 1 coverslip on the bottom with UV-curable glass glue (Norland NOA61). The imaging window and a head plate (Luigs & Neumann) were attached to the skull with cyanoacrylate gel (UHU SuperGel). Dental cement (Super Bond C&B, Sun Medical) was then applied until the complete closure of the cranial surgery. As before, animals were provided with care after the end of the surgery and could recover for at least two weeks before the beginning of experiments.

Two-photon imaging. Mice were progressively handled and habituated to the imaging setup and head fixation for at least one week before starting imaging experiments. Additional habituation sessions were occasionally added until the mice showed no more signs of stress, usually expressed as uninterrupted and disorganized runs. Mice were placed on a 2m-long linear treadmill (Luigs & Neumann) for close-loop experiments described below. Using a treadmill, we could better monitor motion that can lead to out-of-focus signal, discarding those frames for analysis while maximizing the number of trials without motion artefacts. Moreover, a treadmill was chosen, since this provides the animals with the opportunity to voluntarily move during the imaging session and therefore is less stressful compared to full immobilization. A 633nm laser (Coherent) was connected to the implanted fiber optic on the mouse through two patch cords. From the laser combiner (LightHUB, Omicron), a main patch cord (Doric Lenses, optic fiber 200µm, NA 0.22, 2m long, SMA-SMA) was connected to a patch cord (Doric Lenses, optic fiber 200µm, NA 0.22, 1m long, SMA-MF1.25), which itself was connected to the implanted optic fiber through a dark mating sleeve (Doric Lenses). To avoid light contamination from the optogenetic stimulation, a filter (Semrock, #SP01- 633RU-32) was inserted before the photomultipliers, and the path between the objective and the photomultipliers was further covered with black tissue. The implanted chronic window was centered under the microscope using widefield epifluorescence before two-photon microscopy imaging. jGCaMP7b was excited with a Ti:Sa laser (Chameleon Vision-S, Coherent) tuned to 930 nm at 10 to 40mW through a 40× water immersion objective (Nikon CFI 40×, 0.80 NA, 3.5 mm WD). Single planes (512 × 512 pixels) were acquired at 30 Hz with a resonant scanner using with ScanImage 2017b. In the first session, multiple fields of view (FOV) per mouse were acquired. For each FOV, optogenetic stimulation using a strong protocol (20 trials, 10Hz, 10 pulses of 50ms each, spaced by 5s) was used to evoke neuronal postsynaptic calcium transients. A custom Python script was used to control the laser, to trigger the beginning of the session, and to trigger the onset of each trial. The treadmill was continuously monitored to initiate an optogenetic stimulation trial when the mouse was quiet for at least one second before the onset of the trial. After post-hoc identification of responding neurons as described below, imaging of dendrites of responding neurons was performed 15 days later in consecutive imaging sessions every four days. For this, segments horizontal to the imaging plane on first or second order basal dendrites in close proximity of the soma were chosen. The global signal-to-noise ratio (SNR) from each dendritic segment was calculated as follows: (1) the signal amplitude was estimated by taking the 95th percentile minus the 5th percentile of the dendritic trace, (2) the noise was estimated by calculating the standard deviation of the high-pass filtered dendritic trace (cutoff: 10 Hz), (3) the signal amplitude was divided by the noise estimation. Dendritic segments with a signal-to-noise ratio below 8 for any of the recorded sessions were discarded (average global dendritic SNR: 16.2 and range: 8-44, average global spine SNR: 7.5 and range: 3-32). For each session and each dendrite, subthreshold optogenetic stimulation was performed (40 trials of 3 pulses of 10ms at 10Hz, spaced by 5s). At the beginning of each session, for each mouse, the order of imaged dendrites was shuffled to account for potential influence of the optogenetic stimulation across the session. The lengths of imaging sessions depended on the number of dendrites to as well as the periods of spontaneous running activity of the mouse. The session durations were as follows:

	Mouse #1	Mouse #2	Mouse #3	Mouse #4	Mouse #5
Day 0	133 min	70 min	36 min	54 min	45 min
Day 4	95 min	71 min	22 min	44 min	38 min
Day 8	75 min	64 min	19 min	44 min	34 min
Day 12	54 min	61 min	19 min	40 min	38 min

Day 16	60min	128 min	20 min	34 min	59 min

Histology. Mice were injected with a lethal dose of ketamine and xylazine and transcardially perfused with PBS followed by 4% paraformaldehyde (PFA). Brains were removed and stored in 4% PFA. Brains were sliced at 60µm using a vibratome (VT1000S, Leica). Slices were mounted on microscope slides using an aqueous mounting medium (FluoroMount) and coverslips (1871, Carl Roth). Multi-tile overview images of native fluorescence of the expressed fluorophores were acquired with an epifluorescence microscope (AxioObserver, Zeiss) using the 10x objective (Plan-Apochromat, Zeiss) for slice overviews. For high-resolution images a confocal microscope (LSM 900, Zeiss) with a 20x objective (Plan-Apochromat, Zeiss) was used. For both, preset parameters for eGFP and mCherry were used and gain, light intensity and exposure time were adjusted for each sample.

Data analysis

Image processing. Time series were motion-corrected using Suite2p (version 0.10.2)[58]. The shift between frames from Suite2p was further used to compare between periods of quiescence and locomotion. For dendritic imaging, time(t)-projections from each motion-corrected recording for each day were made. T-projections were registered using the rigid body or translation mode of the plugin StackReg[59] of the open-source platform Fiji[60]. Images were visually inspected and dendrites presenting excessive motion were removed from further analyses. Regions of interest (ROIs) were manually drawn around visually identified spines on motion-corrected frames in Fiji. ROIs were separately drawn for dendrites and the background. Calcium traces were extracted on the motion-corrected frames using a custom-made script by averaging the fluorescence of all pixels of each ROI (Fiji).

Trial selection. All data were analyzed using custom-made scripts with Python (Python Software Foundation) installed on an open-source Anaconda environment (Anon, 2020. *Anaconda Software Distribution*, Anaconda Inc. https://docs.anaconda.com/) and the PyCharm integrated development environment (JetBrains). First, residual motion present in motion-corrected recordings was identified using cross-correlation on the motion-corrected frames and excluded from the analysis. To be considered, trials were required to constitute of at least 1 second of stable baseline (without excessive motion as determined ahead of trial start), and at least 70% of the data points during stimulation needed to be stable.

Fluorescence transient analysis. In time series at the cellular resolution, the extracted fluorescence from Suite2p was used. To correct for fluorescence bleaching and to increase the signal-to-noise ratio in the data, a baseline correction was been applied. For each neuron, the neuropil was subtracted from the raw fluorescence: $F_{neuron} = F_{raw} - 0.7 \times F_{neuropil}$ [30,58,61]. To identify neurons responding to optogenetic stimulation, the average trace of the baseline-corrected calcium signal after stimulation was used for each neuron. A neuron was classified as responding if the fluorescence during more than 50% of the time points during the optogenetic stimulation was greater than 95% of the values of the mean-shuffled ΔF/F (10,000 shuffles, $p < 0.05$).

To identify dendritic transients, the distribution of the ROIs data points for each neuron was used. Using a bootstrap analysis, the null distribution was obtained by permutation of the onset of the optogenetic stimulation at random locations. Then, significant optogenetically-evoked dendritic transients were detected as ΔF/F greater than the ΔF/F obtained from the 95% of the values of the mean-shuffled ΔF/F (10,000 shuffles, $p < 0.05$). A transient was further confirmed if, during the optogenetic stimulation, more than 30% of the data points were significant as described above.

Because suprathreshold calcium events mask the spine-specific calcium transients, robust regression was used to reduce the contamination of dendritic calcium activity on spine calcium

traces, as previously reported[29,30]. To decrease the high-frequency noise in traces, spine calcium traces were convolved using a 5-bin boxcar.

For each spine, an average trace using all trials was used to determine if a spine shows excitatory postsynaptic calcium transients (EPSCaTs). Permutations were made to find statistically significant time points during the optogenetic stimulation window. To minimize false-positive spines due to noise in the signal, as for dendrites, a spine was classified as responding if the calcium signal was greater than 95% of the values of the mean- shuffled ΔF/F (10,000 shuffles, $p < 0.05$) for more than 30% of the time points during the optogenetic stimulation. A spine qualified as responsive if optogenetically-evoked transients were detected in at least one out of the five sessions. Spines for which no significant optogenetically-evoked transients were detected in any of the five sessions were classified as unresponsive.

For the analysis presented in Figure 4f-g, the spines were distributed into the five different categories based on their maximal fluorescent transient during optogenetic stimulation ranging from lowest (in the lowest 25th percentile of all spines), low (between the 25th and 50th percentile of all spines), mid (between the 50th and 75th percentile of all spines), high (between 75th and 95th percentile of all spines) and highest (above 95th percentile of all spines).

Morphological analysis. All spines were visually inspected and annotated for their existence on each day. Spines were then classified into four categories depending on the survival sequences, as follows:

- Formed if appearing in one of the sessions and staying until the end of experiments.
- Eliminated if present since the first session but disappearing during the experiments without reappearing in any of the following sessions
- Persistent if present on all recording days
- Transient if appearing and disappearing during the experiment.

The turnover ratio was calculated as the sum of formed and eliminated spines divided by the number of spines present between the days. The survival fraction at a given day was calculated as the fraction of spines present in the corresponding imaging session that were present in all preceding imaging sessions from the beginning.

Spine densities were obtained by dividing the number of spines present on dendrites by the length of the dendritic segment.

Spine volume. The volume of each spine was estimated as previously reported[7,31]. Briefly, each t-projection was deconvolved using the plugins Diffraction PSF 3D and Iterative Deconvolve 3D[62] (Fiji). All pixels in a spine ROI whose brightness exceeded the mean fluorescence of the background were summed and divided by the average fluorescence of the same number of pixels taken from the closest dendrite ROI. Since the resulting number is a ratio, it is unit-free and spine volume is given in arbitrary units (a.u.).

For estimation of spine volume on the stacks obtained at the isosbestic excitation wavelength, a z- projection was computed from the registered frames (StackReg, Fiji) excluding frames with excessive motion followed by the same strategy as described above.

Spatial spine distribution. The interspine distances were calculated as previously reported[31]. Briefly, the distance between two spines was calculated as the dendritic length between the base of a pair of spines. The mass centers of the spines were projected on the dendrite. A path was then obtained using Dijkstra's algorithm and the resulting distance was converted to micrometers based on a previous field of view measurement on the microscope.

Cell count. Using CellPose[63], cells in the red channel of z-stacks of CA3b confocal images, around the injection site in which ChrimsonR was expressed, were segmented with the Segment Anything

model. Automatically generated ROIs were visually inspected and manually curated. To estimate the number of ChrimsonR-expressing CA3 cells, the density of cells per stack was multiplied by the estimated volume of CA3 (~0.4 mm^3). An average of cell densities across all slices was the obtained for each mouse.

Statistics. Statistical analyses were performed using custom scripts on Python or R Studio (Foundation for Statistical Computing). A custom Python script was used to perform bootstrap analysis with 10,000 random permutations of the data to generate a null distribution. Data points were considered significant if they exceeded 95% of the values from the shuffled distribution. ($p < 0.05$).

Pearson's chi-square tests (function *chisq.test*, stats library) were used to test the significance in case of categorical data (Figure S3), an exact binomial test (function *binom.test*, stats library) was performed to test for the fraction of responsive spines (Figure 2a) and linear mixed models (function *lmer*, lmerTest library) were performed using R Studio. Dendrites were qualified as random effects as indicated in the legend for each test. Pairwise comparisons were corrected with Bonferroni correction.

Data availability. The data that support the findings of this study are available from the corresponding author upon request.

Code availability. The custom code of this study is available from the corresponding author upon request.

REFERENCES

1. Whitlock, J. R., Heynen, A. J., Shuler, M. G. & Bear, M. F. Learning Induces Long-Term Potentiation in the Hippocampus. *Science* **313**, 1093–1097 (2006).

2. Xu, T. *et al.* Rapid formation and selective stabilization of synapses for enduring motor memories. *Nature* **462**, 915–919 (2009).

3. Hayashi-Takagi, A. *et al.* Labelling and optical erasure of synaptic memory traces in the motor cortex. *Nature* **525**, 333–338 (2015).

4. Harris, K. M. & Kater, S. B. Dendritic Spines: Cellular Specializations Imparting Both Stability and Flexibility to Synaptic Function. *Annu. Rev. Neurosci.* 17:341-71 (1994).

5. Nägerl, U. V., Eberhorn, N., Cambridge, S. B. & Bonhoeffer, T. Bidirectional Activity-Dependent Morphological Plasticity in Hippocampal Neurons. *Neuron* **44**, 759–767 (2004).

6. Trachtenberg, J. T. *et al.* Long-term in vivo imaging of experience-dependent synaptic plasticity in adult cortex. *Nature* **420**, 788–794 (2002).

7. El-Boustani, S. *et al.* Locally coordinated synaptic plasticity of visual cortex neurons in vivo. *Science* **360**, 1349–1354 (2018).

8. Noguchi, J. *et al.* In vivo two-photon uncaging of glutamate revealing the structure–function relationships of dendritic spines in the neocortex of adult mice. *J. Physiol.* **589**, 2447–2457 (2011).

9. Squire, L. R. *Memory and Brain*. xiii, 315 (Oxford University Press, New York, NY, US, 1987).

10. Greenough, W. T. & Bailey, C. H. The anatomy of a memory: convergence of results across a diversity of tests. *Trends Neurosci.* **11**, 142–147 (1988).

11. Fauth, M. & Tetzlaff, C. Opposing Effects of Neuronal Activity on Structural Plasticity. *Front. Neuroanat.* **10**, (2016).

12. Holtmaat, A. & Svoboda, K. Experience-dependent structural synaptic plasticity in the mammalian brain. *Nat. Rev. Neurosci.* **10**, 647–658 (2009).

13. Loewenstein, Y., Yanover, U. & Rumpel, S. Predicting the Dynamics of Network Connectivity in the Neocortex. *J. Neurosci.* **35**, 12535–12544 (2015).

14. Gu, L. *et al.* Long-Term In Vivo Imaging of Dendritic Spines in the Hippocampus Reveals Structural Plasticity. https://doi.org/10.1523/JNEUROSCI.1464-14.2014 (2014) doi:10.1523/JNEUROSCI.1464-14.2014.

15. Yang, W. *et al.* Anesthetics fragment hippocampal network activity, alter spine dynamics, and affect memory consolidation. *PLOS Biol.* **19**, e3001146 (2021).

16. Pfeiffer, T. *et al.* Chronic 2P-STED imaging reveals high turnover of dendritic spines in the hippocampus in vivo. *eLife* **7**, (2018).

17. Attardo, A., Fitzgerald, J. E. & Schnitzer, M. J. Impermanence of dendritic spines in live adult CA1 hippocampus. *Nature* **523**, 592–596 (2015).

18. Stujenske, J. M., Spellman, T. & Gordon, J. A. Modeling the Spatiotemporal Dynamics of Light and Heat Propagation for In Vivo Optogenetics. *Cell Rep.* **12**, 525–534 (2015).

19. Klapoetke, N. C. *et al.* Independent optical excitation of distinct neural populations. *Nat. Methods* **11**, 338–346 (2014).

20. Bernard, C. & Wheal, H. V. Model of local connectivity patterns in CA3 and CA1 areas of the hippocampus. *Hippocampus* **4**, 497–529 (1994).

21. Martin, S. J., Shires, K. L. & da Silva, B. M. Hippocampal Lateralization and Synaptic Plasticity in the Intact Rat: No Left–Right Asymmetry in Electrically Induced CA3-CA1 Long-Term Potentiation. *Neuroscience* **397**, 147–158 (2019).

22. Holbro, N., Grunditz, Å., Wiegert, J. S. & Oertner, T. G. AMPA receptors gate spine Ca2+ transients and spike-timing-dependent potentiation. *Proc. Natl. Acad. Sci.* **107**, 15975–15980 (2010).

23. Kovalchuk, Y., Eilers, J., Lisman, J. & Konnerth, A. NMDA Receptor-Mediated Subthreshold Ca2+ Signals in Spines of Hippocampal Neurons. *J. Neurosci.* **20**, 1791–1799 (2000).

24. Sabatini, B. L., Oertner, T. G. & Svoboda, K. The Life Cycle of Ca2+ Ions in Dendritic Spines. *Neuron* **33**, 439–452 (2002).

25. Emptage, N., Bliss, T. V. P. & Fine, A. Single Synaptic Events Evoke NMDA Receptor–Mediated Release of Calcium from Internal Stores in Hippocampal Dendritic Spines. *Neuron* **22**, 115–124 (1999).

26. Emptage, N. J., Reid, C. A., Fine, A. & Bliss, T. V. P. Optical Quantal Analysis Reveals a Presynaptic Component of LTP at Hippocampal Schaffer-Associational Synapses. *Neuron* **38**, 797–804 (2003).

27. Oertner, T. G., Sabatini, B. L., Nimchinsky, E. A. & Svoboda, K. Facilitation at single synapses probed with optical quantal analysis. *Nat. Neurosci.* **5**, 657–664 (2002).

28. Gonzalez, K. C. *et al.* Visually guided in vivo single-cell electroporation for monitoring and manipulating mammalian hippocampal neurons. *Nat. Protoc.* 1–17 (2025) doi:10.1038/s41596-024-01099-4.

29. Iacaruso, M. F., Gasler, I. T. & Hofer, S. B. Synaptic organization of visual space in primary visual cortex. *Nature* **547**, 449–452 (2017).

30. Chen, T.-W. *et al.* Ultrasensitive fluorescent proteins for imaging neuronal activity. *Nature* **499**, 295–300 (2013).

31. Hedrick, N. G. *et al.* Learning binds new inputs into functional synaptic clusters via spinogenesis. https://doi.org/10.1038/s41593-022-01086-6 (2022) doi:10.1038/s41593-022-01086-6.

32. Holtmaat, A. J. G. D. *et al.* Transient and persistent dendritic spines in the neocortex in vivo. *Neuron* **45**, 279–291 (2005).

33. Kasai, H. Unraveling the mysteries of dendritic spine dynamics: Five key principles shaping memory and cognition. *Proc. Jpn. Acad. Ser. B* **99**, 254–305 (2023).

34. Fu, M., Yu, X., Lu, J. & Zuo, Y. Repetitive motor learning induces coordinated formation of clustered dendritic spines in vivo. *Nature* **483**, 92–96 (2012).

35. Sorra, K. E. & Harris, K. M. Occurrence and three-dimensional structure of multiple synapses between individual radiatum axons and their target pyramidal cells in hippocampal area CA1. *J. Neurosci.* **13**, 3736–3748 (1993).

36. Druckmann, S. *et al.* Structured Synaptic Connectivity between Hippocampal Regions. *Neuron* **81**, 629–640 (2014).

37. Hill, D. N., Varga, Z., Ji, H., Sakmann, B. & Konnerth, A. Multibranch activity in basal and tuft dendrites during firing of layer 5 cortical neurons in vivo. *Proc. Natl. Acad. Sci. U. S. A.* **110**, 13618–13623 (2013).

38. Kwon, H.-B. & Sabatini, B. L. Glutamate induces de novo growth of functional spines in developing cortex. *Nature* **474**, 100–104 (2011).

39. Yasumatsu, N., Matsuzaki, M., Miyazaki, T., Noguchi, J. & Kasai, H. Principles of Long-Term Dynamics of Dendritic Spines. *J. Neurosci.* **28**, 13592–13608 (2008).

40. Grutzendler, J., Kasthuri, N. & Gan, W. B. Long-term dendritic spine stability in the adult cortex. *Nature* **420**, 812–816 (2002).

41. Takahashi, N. *et al.* Locally Synchronized Synaptic Inputs. *Science* **335**, 353–356 (2012).

42. Kastellakis, G., Cai, D. J., Mednick, S. C., Silva, A. J. & Poirazi, P. Synaptic clustering within dendrites: An emerging theory of memory formation. *Prog. Neurobiol.* **126**, 19–35 (2015).

43. Sheffield, M. E. J. & Dombeck, D. A. Calcium transient prevalence across the dendritic arbour predicts place field properties. *Nature* **517**, 200–204 (2015).

44. Sheffield, M. E. J., Adoff, M. D. & Dombeck, D. A. Increased Prevalence of Calcium Transients across the Dendritic Arbor during Place Field Formation. *Neuron* **96**, 490-504.e5 (2017).

45. Adoff, M. D. *et al.* The functional organization of excitatory synaptic input to place cells. *Nat. Commun.* **12**, 1–15 (2021).

46. Mainen, Z. F., Malinow, R. & Svoboda, K. Synaptic calcium transients in single spines indicate that NMDA receptors are not saturated. *Nature* **399**, 151–155 (1999).

47. Gonzalez, K. C. *et al.* Synaptic basis of feature selectivity in hippocampal neurons. *Nature* 1–9 (2024) doi:10.1038/s41586-024-08325-9.

48. Wiegert, J. S. & Oertner, T. G. Long-Term depression triggers the selective elimination of weakly integrated synapses. *Proc. Natl. Acad. Sci. U. S. A.* **110**, (2013).

49. Wiegert, J. S., Pulin, M., Gee, C. E. & Oertner, T. G. The fate of hippocampal synapses depends on the sequence of plasticity-inducing events. *eLife* **7**, 1–18 (2018).

50. Sasaki, T., Matsuki, N. & Ikegaya, Y. Heterogeneity and independency of unitary synaptic outputs from hippocampal CA3 pyramidal cells. *J. Physiol.* **590**, 4869–4880 (2012).

51. Roo, M. D., Klauser, P. & Muller, D. LTP Promotes a Selective Long-Term Stabilization and Clustering of Dendritic Spines. *PLOS Biol.* **6**, e219 (2008).

52. Dudek, S. M. & Bear, M. F. Homosynaptic long-term depression in area CA1 of hippocampus and effects of N-methyl-D-aspartate receptor blockade. *Proc. Natl. Acad. Sci. U. S. A.* **89**, 4363–4367 (1992).

53. Williams, L. E. & Holtmaat, A. Higher-Order Thalamocortical Inputs Gate Synaptic Long-Term Potentiation via Disinhibition. *Neuron* **101**, 91-102.e4 (2019).

54. Bittner, K. C., Milstein, A. D., Grienberger, C., Romani, S. & Magee, J. C. Behavioral time scale synaptic plasticity underlies CA1 place fields. *Science* **357**, 1033–1036 (2017).

55. Fan, L. Z. *et al.* All-optical physiology resolves a synaptic basis for behavioral timescale plasticity. *Cell* S0092867422015781 (2023) doi:10.1016/j.cell.2022.12.035.

56. Castello-Waldow, T. P. *et al.* Hippocampal neurons with stable excitatory connectivity become part of neuronal representations. *PLoS Biol.* **18**, (2020).

57. Sohn, J. *et al.* Presynaptic supervision of cortical spine dynamics in motor learning. *Sci. Adv.* **8**, eabm0531 (2022).

58. Pachitariu, M. *et al.* Suite2p: beyond 10,000 neurons with standard two-photon microscopy. Preprint at https://doi.org/10.1101/061507 (2016).

59. Thevenaz, P., Ruttimann, U. E. & Unser, M. A pyramid approach to subpixel registration based on intensity. *IEEE Trans. Image Process.* **7**, 27–41 (1998).

60. Schindelin, J. *et al.* Fiji: an open-source platform for biological-image analysis. *Nat. Methods* **9**, 676–682 (2012).

61. Peron, S. P., Freeman, J., Iyer, V., Guo, C. & Svoboda, K. A Cellular Resolution Map of Barrel Cortex Activity during Tactile Behavior. *Neuron* **86**, 783–799 (2015).

62. Dougherty, R. Extensions of DAMAS and Benefits and Limitations of Deconvolution in Beamforming | Aeroacoustics Conferences. *Adv. Test. Tech. Phased Arrays* https://doi.org/10.2514/6.2005-2961 (2012) doi:https://doi.org/10.2514/6.2005-2961.

63. Stringer, C., Wang, T., Michaelos, M. & Pachitariu, M. Cellpose: a generalist algorithm for cellular segmentation. *Nat. Methods* **18**, 100–106 (2021).

ACKNOWLEDGMENTS

We thank Maxime Maheu for help with data analyses, Stefan Schillemeit and Kathrin Sauter for excellent technical support, Wei Yang for initial training on spine imaging and Michael D. Adoff and Daniel A. Dombeck for advice on cranial window surgery. Ingke Braren of the UKE Vector Facility produced rAAV vectors. This work was supported by European Research Council (ERC2016-StG-714762 to J.S.W.) and the German Research Foundation, DFG (project numbers: 273915538 - SPP1926 and 278170285 - FOR2419/P6, to J.S.W.).

AUTHOR CONTRIBUTIONS

C.R. and J.S.W. designed the experiments and wrote the manuscript. C.R. performed the experiments and analyzed the data. J.S.W. acquired funding and supervised the study.

SUPPLEMENTAL FIGURES

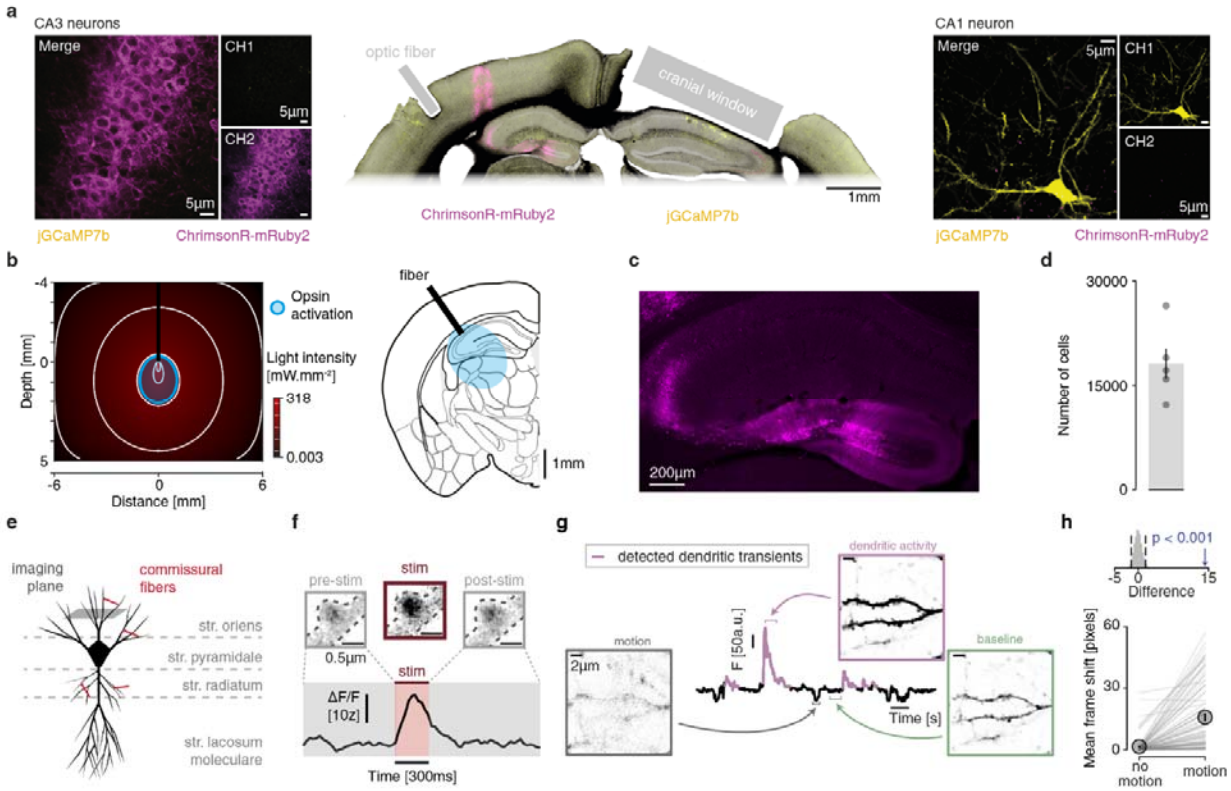

Figure S1. Imaging of spines in CA1. a) Expression of ChrimsonR and jGCaMP7b. Left: clCA3 neurons expressing ChrimsonR-mRuby2 (magenta, CH1). Right: ilCA1 neurons sparsely expressing jGCaMP7b (yellow, CH2). Middle: Macroscopic overview of a brain section showing positions of optic fiber for stimulation above clCA3 and the chronic imaging window above ilCA1. **b)** Monte-Carlo simulation of light propagation from the tip of the optic fiber in the mouse brain. The area which was illuminated with sufficient irradiance to activate ChrimsonR (blue outline, left) is depicted in blue as an overlay on a section from the Allen brain atlas (right). **c)** Confocal image of brain section from contralateral hippocampus showing expression of ChrimsonR-mRuby2. **d)** Estimated total number of cells in CA3 expressing ChrimsonR. Each datapoint is the average number of cells per mouse (n = 5 mice). **e)** Schematic drawing of an ilCA1 neuron showing the imaging plane in stratum oriens. **f)** Example calcium trace of a single EPSCaT with corresponding t-projections of the spine before, during and after optogenetic stimulation. **g)** Example trace of dendritic fluorescence including bouts of locomotion. Calcium events are marked in pink. Average z-projections are shown for baseline fluorescence (right, green) and for a dendritic calcium transient (magenta, top right). Motion events led to out-of-focus signal (left inset, gray frame). **h)** Quantification of frame shift during immobility and motion. Top: Permutation test. Arrow represents the true difference.

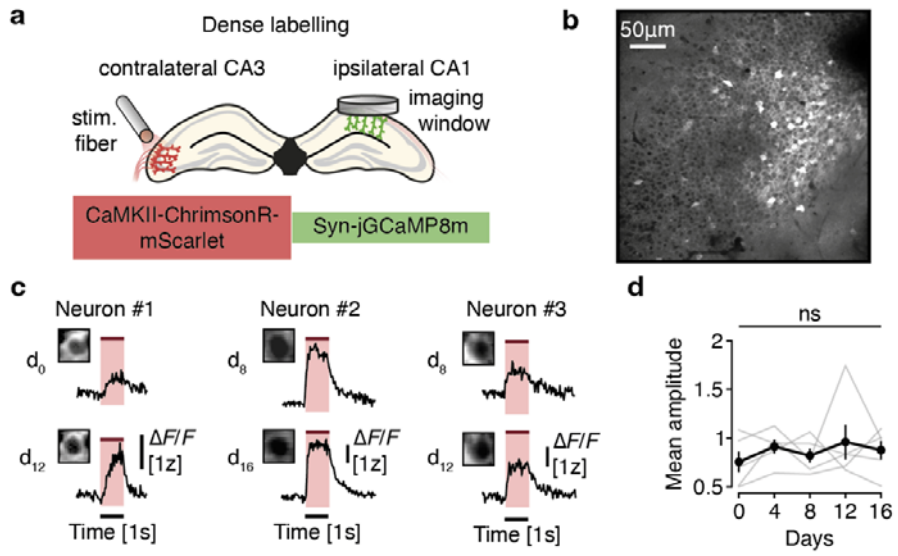

Figure S2. Stable optogenetic stimulation of iICA1 over the time course of the experiment. a) Schematic illustration depicting the injections and chronic implants for dense labelling of iICA1 with jGCaMP8m. **b)** Example field of view with densely labelled neurons in iICA1. **c)** Average postsynaptic calcium responses from three example neurons at two timepoints (d0 and d12). **d)** Average mean amplitude of postsynaptic calcium responses over the time course of the experiment for all responding neurons (n = 5 mice, 387 neurons). Linear Mixed Model with dendrites as random effect. ns: non-significant. Mean ± s.e.m.

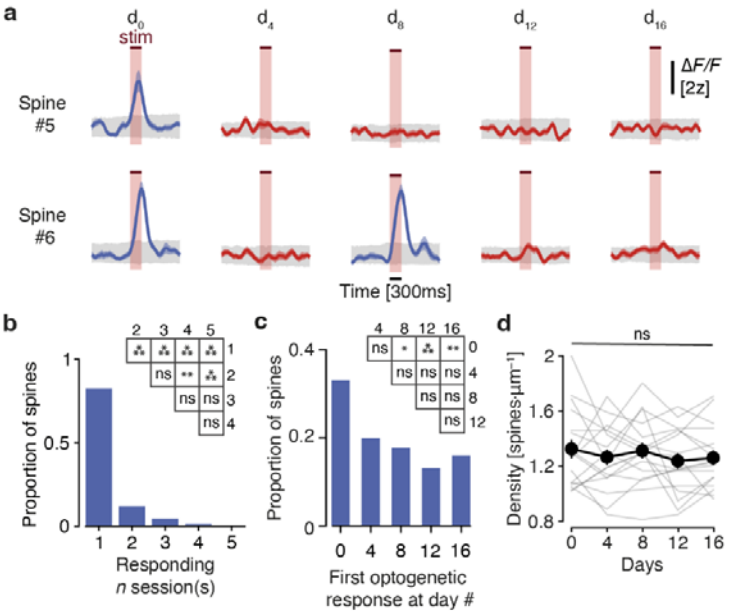

Figure S3. The majority of responsive spines show EPSCaTs only in one session. a) Examples of responding status changes over time. Spine #5 was responding in one session (d0) while spine #6 was responding in two sessions at days 0 and 8. Mean ± s.e.m. **b)** Distribution of spines according to the number of sessions in which they showed a response. Pairwise chi- square tests are shown in the table. **c)** Distribution of spines according to the sessions in which they showed a response for the first time. Pairwise chi- square tests are shown in the table. **d)** Average spine density on all recorded dendrites. Linear mixed model, dendrites are random effects. *: p < 0.05, **: p < 0.01, ***: p < 001, ns: non-significant. Mean ± s.e.m.

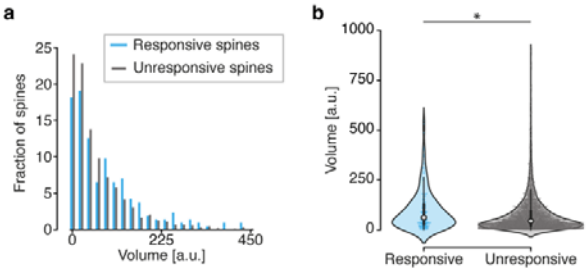

Figure S4. The volume of responsive spines is higher than the volume of unresponsive spines. a) Histogram of the distribution of the volume of responsive (blue) and unresponsive (grey) spines as in Figure 2c. 22 bins equally spaced (20a.u.) were used. **b)** Volumes of all responsive and unresponsive spines. Permutation tests. *: $p < 0.05$.

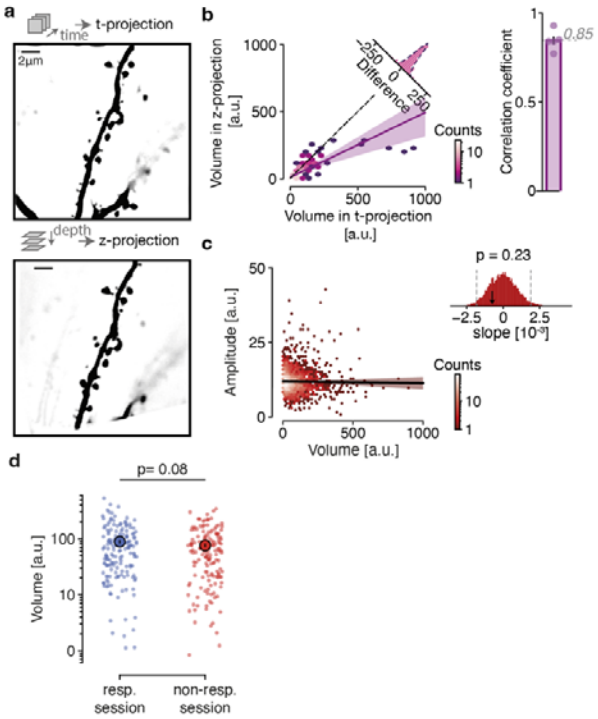

Figure S5. Spine volume estimated from the time series is independent of calcium activity. a) Example projections of the same dendrite from the time-series (t-projection) and from the stack (z-projection). **b)** Volume estimated from z-projections as a function of the volume estimated from t-projections for all spines (n=164 spines, 4 dendrites, 5 sessions). The high correlation coefficient indicates that both methods yield similar volume estimates. **c)** Spine head volume as a function of EPSCaT amplitudes in the respective spines. Absence of correlation indicates that EPSCaTs and spine volume can be measured independently. Permutation tests. **d)** Volume of responsive spines separately plotted for responding and non-responding sessions. Linear Mixed Model with spines as random effect. N= 175 responsive spines, 17 dendrites, 5 mice. ***: $p < 0.001$, ns: non-significant.

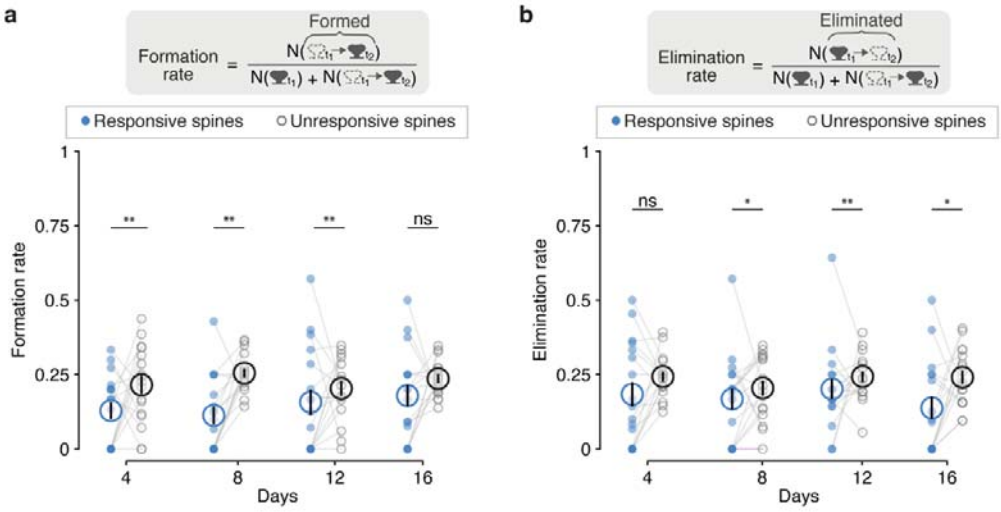

Fig S6. Both formation and elimination rates are different between responsive and unresponsive spines. a) Formation rate and **b)** elimination rate of responsive spines versus unresponsive spines over time. Linear Mixed Model with dendrites as random effect and pairwise comparisons with Bonferroni correction. Mean ± s.e.m. N=175 responsive and 754 unresponsive spines, 17 dendrites, 5 mice.

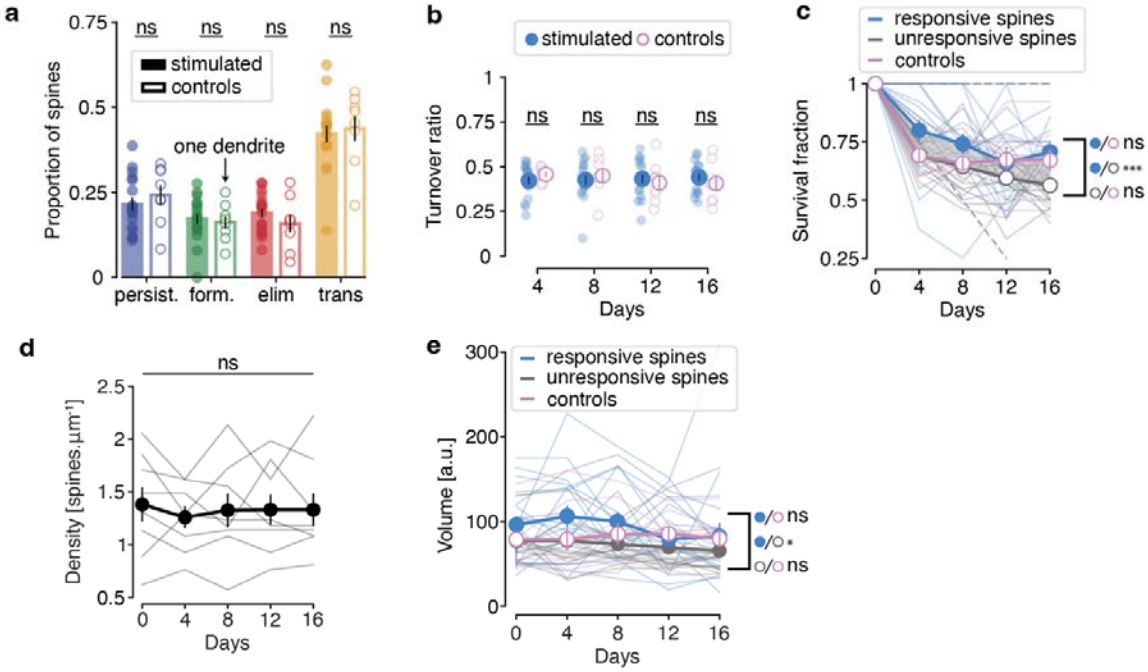

Figure S7. Optogenetic stimulation does not affect the overall stability or volume of dendritic spines. a) Proportion of different dynamic spine categories on dendrites in control animals (no optogenetic stimulation, N= 8 dendrites) and optogenetically-stimulated animals (N=17 dendrites). Linear Mixed Model and pairwise comparisons with dendrites as random effect. . Mean ± s.e.m. Each dot represents one dendrite. **b)** Turnover ratio of stimulated dendrites and controls over time. Linear Mixed Model and pairwise comparisons with dendrites as random effect. Mean ± s.e.m. **c)** Survival fractions of control, responsive and unresponsive spines. Linear Mixed Model, dendrites are random effects and responsive, unresponsive and control as fixed effects. Mean ± s.e.m. **d)** Density of spines from control animals. Linear Mixed Model with dendrites as random effects. Mean ± s.e.m. **e)** Volumes of control, responsive and unresponsive spines. Linear Mixed Model with dendrites as random effect and pairwise comparisons. Mean ± s.e.m. ***: $p < 0.001$, *: $p < 0.05$, ns: non-significant.

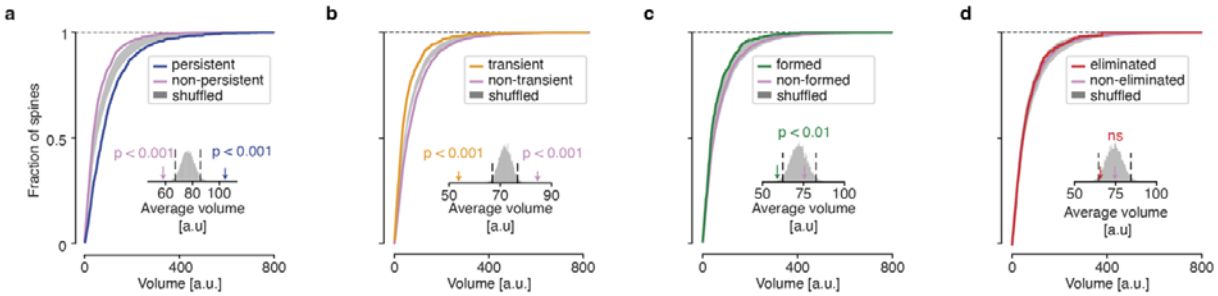

Fig S8. Stable spines have larger head volumes. Cumulative distributions of the head volumes of persistent (**a**), transient (**b**), formed (**c**) and eliminated (**d**) spines versus spines of all other categories (pink). Shuffled volumes are indicated in shaded grey. Permutation tests. Arrows indicate actual average spine volumes of the respective categories.

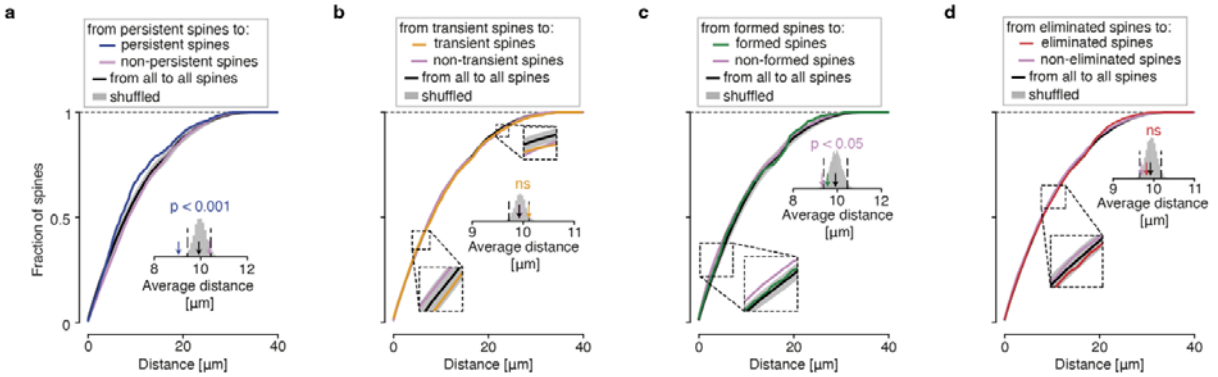

Fig S9. Persistent spines show higher proximity to each other than non-persistent spines. a) - d) Cumulative distributions of distances between persistent, transient, formed, and eliminated spines, compared to the distances to the other spines. Shuffled distances are indicated in shaded grey. Arrows indicate actual average distance between spines of the respective categories. Permutation tests.